RESEARCH PAPER

Fouling and its mitigation in silicon microchannels used for IC chip cooling

Jeffrey L. Perry · Satish G. Kandlikar

Abstract Particulate fouling studies with alumina dispersions in water were performed in rectangular, silicon microchannels having hydraulic diameters between 220 and 225 μm with Reynolds numbers of 17–41. Data show for the most part the absence of particle deposition within the microchannels. The primary reason for this is the relatively high wall shear stress at the microchannel walls of 2.3–3.5 Pa compared to conventional size passageways. In contrast, the headers for the microchannels are quite susceptible to particulate fouling under the same conditions. This is because the shear stress in the header region is lower. Proper adjustment of pH has been identified to effectively mitigate the fouling by controlling the electrostatic forces of repulsion between particle–particle interactions.

Keywords Fouling · Microchannels · Particulates · pH · Shear stress

List of symbols

a	particle radius (m)
A_{132}	Hamaker constant (J)
b	half channel width (m)
c	half channel height (m)
d, d_p	particle diameter (m)
D_h	hydraulic diameter (m)
e	elementary electric charge (coulomb)
E_{el}	electrostatic interaction energy (J)
E_t	total interaction energy (J)
E_{vdw}	van der Waals interaction energy (J)
F_{el}	electrostatic force (N)
F_g	gravitational force (N)
F_L	lift force (N)
F_T	total force (N)
F_{vdw}	Van der Waals force (N)
g	acceleration due to gravity (m/s^2)
H	minimum separation distance (m)
J_B	collision rate due to Brownian motion (1/s)
J_S	collision rate due to shear (1/s)
k	Boltzmann constant (J/K)
m, n	exponents (unitless)
n^*	electrolyte concentration (atom or molecule per m^3)
Re	Reynolds number (unitless)
R_{ij}	collision radius of particles i and j (m)
R_p	particle radius (m)
s	half fin width (m)
T	absolute temperature (K)
u, U	velocity (m/s)
u_m	mean velocity (m/s)
u_{max}	maximum velocity (m/s)
y, z	distance from surface (m)
z^*	electrolyte valance charge (unitless)

Greek symbols

α_c^*	channel aspect ratio (unitless)
δ^*	parameter in determining zeta potential (unitless)
ε_o	dielectric permittivity of vacuum (F/m)
ε_r	relative dielectric constant of medium (unitless)
κ	Debye–Hückel parameter (1/m)
$1/\kappa$	Debye length or diffuse layer thickness (m)
λ	wavelength (m)
λ_c	characteristic wavelength of interaction (m)

J. L. Perry
Microsystems Engineering, Rochester Institute of Technology, Rochester, NY 14623, USA

S. G. Kandlikar (✉)
Department of Mechanical Engineering,
Rochester Institute of Technology, Rochester, NY 14623, USA
e-mail: sgkeme@rit.edu

μ_E	electrophoretic mobility (m^2/V s)
μ_f	viscosity of fluid (kg/m s)
ρ_f	density of fluid (kg/m^3)
ρ_p	density of particle (kg/m^3)
τ_w	Shear stress at wall (Pa)
ψ_s	surface potential (V)
ζ	zeta potential (V)

1 Introduction

Microfluidics is an increasingly studied field because of its use in practical applications in both biology and microelectronics. In recent years, the proliferation of Micro Electro Mechanical Systems (MEMS) has resulted in the use of microchannels for many applications. In particular, with microchannels there has been a great emphasis on semiconductor chip cooling. Consequently, it is desirable to study the effect of particulates in such devices, which must operate over the lifetime of the semiconductor chip.

The smallest hydraulic diameters, D_h, that have been previously used in fouling studies that the authors are aware of were by Benzinger et al. (2005). Their microstructured heat exchanger had a $D_h = 178$ µm. Their studies focused on crystallization fouling using aqueous solutions of Ca(NO$_3$)$_2$/NaHCO$_3$. However, crystallization fouling is an unlikely occurrence in microchannels used for heat dissipation as it relates to semiconductor chip cooling.

Concerning particulate depositions, however, the smallest hydraulic diameters used were in the studies of Yiantsios and Karbelas (1995, 1998, 2003) and Niida et al. (1989). Yiantsios et al. studied fouling in a single channel with $D_h = 952$ µm. Their test section consisted of two glass plates separated by Teflon spacer strips to create a channel that was 10 mm by 0.5 mm. Similarity, Niida et al. used an observation cell, made of borosilicate glass with a cross-section of 4 mm by 0.4 mm to provide a D_h of 727 µm. In the present fouling studies microchannels are being used which have dimensions of 249 µm × 205 µm ($D_h = 225$ µm) and 407 µm × 151 µm ($D_h = 220$ µm).

In a similar vain to particulate depositions in microchannels is work done by Bergendahl and Grasso (2000). Their efforts focused on modeling and understanding the mobility of colloids through porous media. To do this they studied the physical detachment of polystyrene colloids affixed to glass beads in a packed column. In addition, Marshall (2007) performed soft-sphere discrete-element computations to examine particle aggregation formation and aerosol capture by walls in laminar microchannel flow. This was performed because adhesive particulates have been identified as a leading cause of failure in many different microfluidic devices.

In general, particulate fouling may be considered a two-step process. It consists of a transport step, in which particles are transferred to the channel wall, and a subsequent adhesion step, which is dominated by the interaction forces between particles and the wall. An important parameter in both steps is the particle size. It is a critical parameter that determines their attachment efficiency. In fact, the particle size affects the magnitude of physicochemical interactions between particles and a channel wall as well as the hydrodynamic forces that tend to cause particles to detach or prevent them from adhering.

2 Background

2.1 Forces on a particle

When a particle is in near contact with a horizontal channel wall, many forces around the particle are involved in determining whether or not adhesion will occur. In this study the forces are categorized into two general main groups. The first group is the adhesive forces, which are due to van der Waals force, F_{vdw}, and gravity, F_g. The second group is the removal forces, which include the hydrodynamic lift force, F_L, and electrostatic force, F_{el}. Typically the electrostatic forces are adjusted to be repulsive. However, the electrostatic forces in actuality may be attractive or repulsive in nature by adjusting the pH of the aqueous medium. If it is made attractive, the sign will change for the electrostatic force in Eq. 1. A schematic showing all these forces is given in Fig. 1. The total force, F_T, on a particle is the sum of the adhesive and removal forces which is expressed as
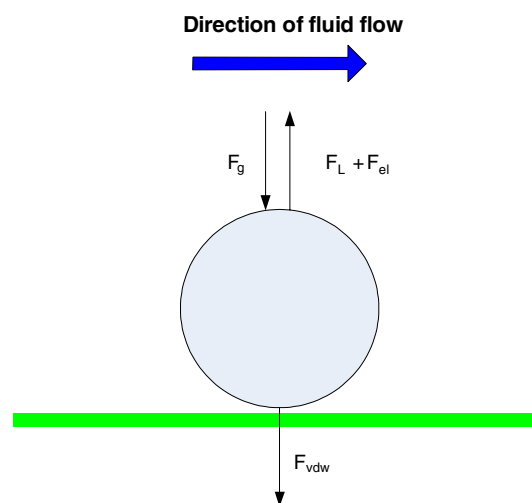

Fig. 1 Schematic showing the attractive and repulsive forces on a particle in near contact with a horizontal channel wall

$$F_{\mathrm{T}} = F_{\mathrm{vdw}} + F_{\mathrm{g}} - F_{\mathrm{el}} - F_{\mathrm{L}} \tag{1}$$

An important aspect that requires addressing is the fact this paper is looking at the attachment of a particle rather than its detachment. In doing so, particle breakaway from the surface is not being studied which includes such forces as (a) the fluid drag force on the particle and the associated resistance to rolling which counteracts it, (b) the change in contact area of a deposited particle caused by particle deformation and (c) the shape of an aggregate attached to a surface.

2.2 Van der Waals force on a particle near a wall

The van der Waals force between a sphere and a plate, which takes into account retardation effects is given by Gregory (1981).

$$F_{\mathrm{vdw}} = \frac{A_{132} d_{\mathrm{p}}}{12 H^2} \left[1 - \frac{1}{1 + \frac{\lambda_{\mathrm{c}}}{(5.32 H)}} \right], \quad H << \frac{d_{\mathrm{p}}}{2} \tag{2}$$

A_{132} is the Hamaker constant of surface 1 and surface 2 in medium 3 ($A_{132} = 5.2 \times 10^{-20}$ J for Si-Al$_2$O$_3$, 3.2×10^{-20} J for Al$_2$O$_3$-Al$_2$O$_3$); (Holmberg 2001; Kern 1993), d_{p} is the particle diameter, H the minimum separation between the particle and the wall, and λ_{c} is the characteristic wavelength of interaction which is taken as ≈ 100 nm for most materials, Gregory (1981).

2.3 Gravity

Gravity in the context of this paper is considered to be an adhesive force. This is because on a horizontal surface it can drive a particle to be in contact with it. The force of gravity of a particle in water is given as

$$F_{\mathrm{g}} = \frac{\pi d_{\mathrm{p}}^3 (\rho_{\mathrm{p}} - \rho_{\mathrm{f}}) g}{6} \tag{3}$$

where ρ_{p} is the density of the particle, ρ_{f} is the density of the fluid and g is the acceleration due to gravity. The gravitation force, is however negligible for nano-sized particles in comparison to the electrostatic and van der Waals forces that are typically present. However, if particles aggregate to tens of microns it can be an important factor.

2.4 Electrostatic force on a particle near a wall

The DLVO theory developed by Derjaguin and Landau (1941), Verwey and Overbeek (1948), independently describes the interaction that takes place when two of these double-layers interpenetrate. Hogg et al. (1966) were

amongst others that extended the DLVO theory to the interaction of dissimilar plates and dissimilar spheres at constant surface potential. Their simplified formulas are however only good for surface potentials up to ≈ 40 mV. Ohshima et al. (1982) came up with analytical expressions that can be applied to higher surface potentials as is the case here.

The analytical expressions developed by Oshima et al. (1982) which describe the force between a sphere and a plate are quite lengthy. Therefore, only the first part of the expression is given. The comprehensive results can be obtained by differentiating Eqs. 49–51 presented by Oshima et al. with respect to H and taking the limit as one of the radii goes to infinity ($F_{\mathrm{el}} = -\mathrm{d}E_{\mathrm{el}}/\mathrm{d}H$, where E_{el} is the electrostatic interaction energy). The force for a symmetrical electrolyte is

$$
\begin{aligned}
F_{\mathrm{el}} &= \frac{4\pi d_{\mathrm{p}} n^* k T e^{-\kappa H}}{\kappa} \left[\frac{Y_+^2}{1 + e^{-\kappa H}} - \frac{Y_-^2}{1 - e^{-\kappa H}} \right] \\
Y_+ &= \frac{y_{s1} + y_{s2}}{2}, \quad Y_- = \frac{y_{s1} - y_{s2}}{2} \\
y_{s1} &= \frac{z^* e}{kT} \psi_{s1}, \quad y_{s2} = \frac{z^* e}{kT} \psi_{s2} \\
\kappa &= \sqrt{\frac{e^2}{\varepsilon_{\mathrm{r}} \varepsilon_{\mathrm{o}} kT} \sum n_i^* z_i^{*2}}
\end{aligned} \tag{4}
$$

where n^* is the electrolyte concentration, k is the Boltzmann constant, T is the absolute temperature, z^* is the electrolyte valance charge, e is the elementary electric charge, κ is the Debye–Hückel parameter of the electrolyte solution (where $1/\kappa$ is known as the Debye length or diffuse layer thickness), ψ_{s1} and ψ_{s2} are the respective surface potentials involved, ε_{r} is the dielectric constant of the medium, and ε_{o} is the dielectric permittivity of a vacuum.

2.5 Hydrodynamic lift force on a particle near a wall

The hydrodynamic lift force for a spherical particle in the vicinity of the deposition surface can be determined by the results of Leighton and Acrivos (1985) who extended the analysis of O'Neill (1968) by taking into account weak inertial effects. They found that the lift force on a spherical particle in contact with a fixed plane wall, in a slow linear shear flow is

$$F_{\mathrm{L}} = 0.58 \rho_{\mathrm{f}} \left(\frac{\tau_{\mathrm{w}}}{\mu_{\mathrm{f}}} \right)^2 d_{\mathrm{p}}^4 \tag{5}$$

where μ_{f} is the viscosity of the fluid and τ_{w} is the shear stress at the wall. This expression is valid for sufficiently small particle Reynolds numbers which are much less than 1. In addition, it can be used to closely approximate the lift force with a separation distance of tens of nanometers.

If one desires to know the average wall shear stress in the header, or the same quantity in the microchannels, relative to the channel/surface bottom, a different approach is necessary. In this case what is desired is the bottom wall shear stress, which can be expressed by Newton's law of viscosity given as

$$\tau_w = \mu_f \left(\frac{du}{dz} \right)_w \tag{6}$$

Here the quantity in parentheses is the velocity gradient at the wall also known as the shear rate. Using Eqs. 5 and 6 it is possible to ascertain the lift force on a bottom surface of the silicon test device. The shear rate within a rectangular duct as expressed by Eq. 6 can be known by determining the velocity profile close to the channel surfaces. This is done using Eqs. 7–9 from Kakaç (1987) for a fully developed flow within a rectangular duct. In this case the velocity profile u is given as

$$\frac{u}{u_{max}} = \left[1 - \left(\frac{y}{b} \right)^n \right] \left[1 - \left(\frac{z}{c} \right)^m \right] \tag{7}$$

$$\frac{u_{max}}{u_m} = \left(\frac{m+1}{m} \right) \left(\frac{n+1}{m} \right) \tag{8}$$

$$m = 1.7 + 0.5\alpha_c^{*-1.4}$$

$$\begin{array}{ll} n = 2 & \text{for} \quad \alpha_c^* \leq \frac{1}{3} \\ n = 2 + 0.3\left(\alpha_c^* - \frac{1}{3} \right) & \text{for} \quad \alpha_c^* \geq \frac{1}{3} \end{array} \tag{9}$$

where u_{max} is the maximum velocity at the center of the channel and α_c^* is the aspect ratio of the channel which must be less than unity. The dimensions for the variables b, c, y and z are provided in Fig. 2 which possesses symmetry along the central axis. Using these equations yields velocity profiles that are within 1% of those computed using more exact relations, Kakaç (1987). With the above equations it is possible to easily determine the average velocity over the entire width of a microchannel for a given distance z from the surface. This is given in Eq. 10

$$\overline{U(y)} = \frac{u_{max}}{b} \int_0^b \left[1 - \left(\frac{y}{b} \right)^n \right] \left[1 - \left(\frac{c-z}{c} \right)^m \right] dy \tag{10}$$

where both b and c are half the channel width and half the channel height respectively.

2.6 Potential energy curves

In classical DLVO theory the total force between a particle and wall is the sum of the repulsive electrostatic forces and attractive van der Waals forces. It is common to describe the force balance between F_{vdw} and F_{el} in the form of a
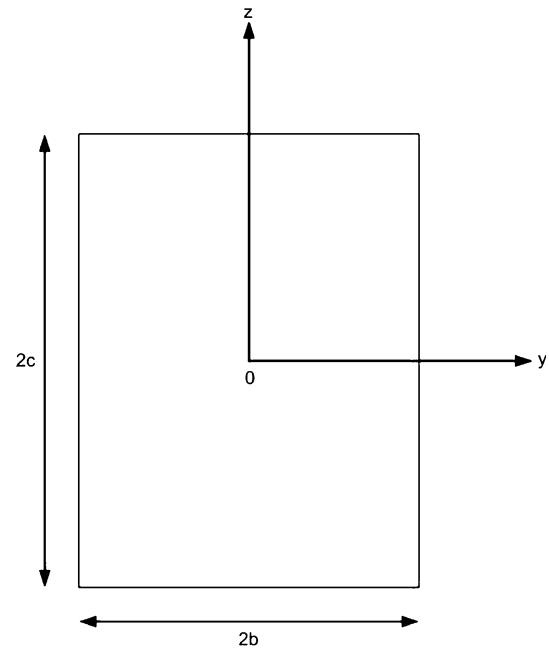

Fig. 2 Coordinate system for a rectangular duct using Eqs. 7–9

potential energy-distance diagram shown in Fig. 3. The total potential energy of interaction, E_t, is given as

$$E_t(H) = E_{vdw}(H) + E_{el}(H) \tag{11}$$

where E_{vdw} and E_{el} are the energies associated with the van der Waals and electric double-layer interactions, respectively.

Equations 12 and 13 give the interaction energies for the van der Waals and electrostatic forces between a particle and a flat plate. These are the formulas from which Eqs. 2 and 4 were derived.

$$E_{vdw}(H) = -\frac{A_{132}d_p}{12H} \left(1 - \frac{5.32H}{\lambda_c} \ln \left(1 + \frac{\lambda_c}{5.32H} \right) \right) \tag{12}$$
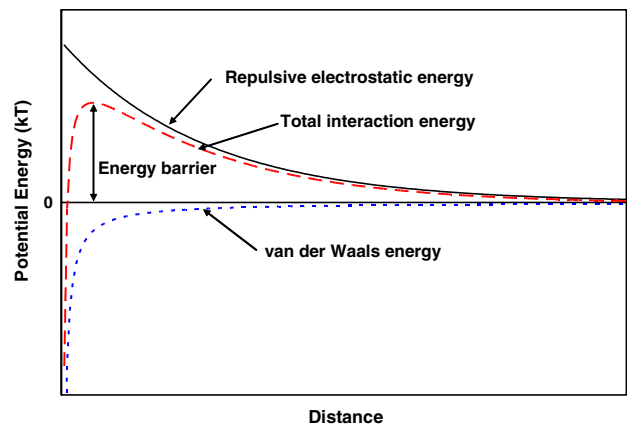

Fig. 3 Potential energy–distance diagram

$$E_{\text{el}}(H) = \frac{4\pi d_{\text{p}} n^* kT}{\kappa^2}\left(Y_+^2 \ln(1 + e^{-\kappa H}) + Y_-^2 \ln(1 - e^{-\kappa H})\right) \tag{13}$$

Additionally, the interaction energies for two particles of diameter d_1 and d_2 which are approaching each other are given by Eqs. 14 and 15 as

$$E_{\text{vdw}}(H) = -\frac{A_{132} d_1 d_2}{12(d_1 + d_2)H}\left(1 - \frac{5.32H}{\lambda_{\text{c}}} \ln\left(1 + \frac{\lambda_{\text{c}}}{5.32H}\right)\right) \tag{14}$$

$$E_{el}(H) = \frac{4\pi d_1 d_2 n kT}{\kappa^2(d_1 + d_2)}\left(Y_+^2 \ln(1 + e^{-\kappa H}) + Y_-^2 \ln(1 - e^{-\kappa H})\right) \tag{15}$$

As a result of the differences in the potential energy-distance relationships for the van der Waals and electric double-layer interactions, the total energy shows a maximum at short separation distances, provided the force of repulsion is sufficiently large. In fouling, this maximum represents an energy barrier to the transport of a particle to a heat exchanger wall. Potential energies are often expressed in units of kT. A barrier height of 10 kT or more implies a very stable situation where only a minute fraction of the particles will have sufficient energy to surmount the energy barrier due to Brownian motion, Van de Ven (1989). If the barrier is overcome, then a particle will be held by van der Waals attraction in the deep primary minimum where removal is less likely.

According to DLVO theory higher surface potentials and a lower ionic strength of the fluid are desirable. This will aid in raising the energy barrier, which should in principle help to minimize fouling. In reality, the mitigation of fouling is more complex because other interactions are possible.

One of these possible interactions is orthokinetic aggregation, which is the formation of aggregates under a shearing force. This is usually associated with agitation. However, the shear rate in microchannels can be significant enough to cause increased particle-particle interactions, which can lead to agglomeration. In the absence of a repulsive energy barrier the ratio of the collision rate due to Brownian motion, J_{B}, and due to shear, J_{S}, is given in Eq. 16

$$\frac{J_S}{J_B} = \frac{\mu_{\text{f}} R_{ij}^3 (\mathrm{d}u/\mathrm{d}z)}{2kT} \tag{16}$$

where R_{ij} is the collision radius of particles i and j ($R_{\text{ij}} \approx 2R_{\text{p}}$).

2.7 Additional aspects in particulate fouling

This section covers other aspects, which are important to particulate fouling but fall outside the force balance and potential energy curves discussed previously. They however can have a direct influence on particle deposits within a microchannel device.

2.7.1 Impaction at wall headers

Particle interception can be an important aspect in particulate fouling. This is especially true when dealing with a heat exchanger with parallel microchannels connected with an inlet manifold. In this phenomenon, a particle can collide with the cross-sectional area of a fin structure and be collected (become trapped). After which, additional particles can be amassed until significant blockage has occurred at the channel entrances. After considerable buildup, the fluid flow into the channels can be impeded by a reduction in the cross-sectional area at the channel inlets. In addition, it is possible for this phenomenon to have a larger impact when the fins make up a larger contribution of the total cross-sectional area in the header region.

2.7.2 Particle agglomeration due to pump effects

The type of pump used in an experimental system can have a significant effect on particle agglomeration. If a pump produces high shear within it, particle agglomeration can occur. A peristaltic pump is one type of pump which helps to avoid this issue. Peristaltic pumps have a low shear action and are often used in the transport of highly concentrated slurries at low flow rates, Abulnaga (2002). The pump provides a straight flow path with no dead zone areas for particles to agglomerate or harden, Hu (2004). Peristaltic pumps however do not provide a pulseless flow. The rollers in the pump head produce a flow that has pulsations. The magnitude of these pulsations, however, can be reduced by having a pump head with a larger number of rollers. In addition, the tubing must be periodically replaced because the rollers wear down the peristaltic tubing over an extended period of time. Thus tradeoffs need to be made when selecting a pump for use in fouling studies with dispersions which may be shear-sensitive.

3 Experimental

3.1 Materials and methods

Two different particle types were used. They are listed in Table 1. The 1.25-μm alumina particles came from Nanostructured and Amorphous Materials, Inc. while the 248-nm alumina particles came from Alfa Aesar. Scanning electron micrographs of each particle type was performed showing randomly shaped, nonspherical structures. An

Table 1 Physical properties of alumina and silicon particles used in fouling or zeta potential measurements

Particle type	α-Al$_2$O$_3$	γ-Al$_2$O$_3$	Si
Average particle size	1.25 μm	248 nm	818 nm
Standard deviation	0.087 μm	1.6 nm	91 nm
Average density (g/cm^3)	3.97	3.97	NA
Percent purity	99.97	99.97	98

additional particle type was silicon from Alfa Aesar. It was not employed in fouling experiments but it was used to help determine the zeta potential of the silicon microchannels under different pH conditions.

Particle size analysis was performed using a Brookhaven 90 Plus particle size analyzer which is based on dynamic light scattering theory. Dispersions of alumina and silicon particles were assisted by using a Branson 200 ultrasonic cleaner. The sonicator helped break up agglomerates so that all the particles would be well dispersed. Moreover, all dispersions for the test were made to 150 g total mass.

Dispersions that were tested had a significant particle concentration by weight. The weight percent of the particles was much higher than would actually be seen in any microchannel device used for IC chip cooling. Therefore, in a practical way all the tests considered were accelerated. This is why data could be collected within only a few hours of operation during the experimental runs.

A Brookhaven 90 Plus with a BI-Zeta zeta potential analyzer was used to obtain the electrophoretic mobility of the charged particles. The temperature during operation within the measurement cell was maintained at room temperature (23 ± 1°C). When calculating zeta potentials from electromobility measurements, care must be taken to use the correct procedure based on the magnitude of κa, where a is the particle radius and κ is the Debye–Hückel parameter. An expression from Oshima (1994) was used to convert electrophoretic mobility to zeta potential which is given as

$$\zeta = \frac{3 u_E \mu_f}{2 \varepsilon f(\kappa a)} \tag{17}$$

where u_E is the electrophoretic mobility and $f(\kappa a)$ is a monotonically varying function which increases from 1.0 at $\kappa a = 0$ to 1.50 at $\kappa a = \infty$. $f(\kappa a)$ is expressed as

$$f(\kappa a) = 1 + \frac{1}{2[1 + \delta^*/\kappa a]^3} \tag{18}$$

where

$$\delta^* = \frac{2.5}{1 + 2 e^{-\kappa a}} \tag{19}$$

A high magnification Keyence digital microscope, model VXH-500 was used to visualize the fouling

phenomena within the microchannel test device. The microscope used a Keyence VH-Z100 wide-range zoom lens with a 10X zoom covering a 100X to 1000X magnification.

Particulate fouling was studied using the flow loop schematic given in Fig. 4. A peristaltic pump (Cole-Parmer Masterflex L/S) was used to drive the fluid, which has a rated speed control of ±0.25%. With a standard Cole-Parmer L/S 14 pump head it can deliver a volumetric flow rate between 1.3 and 130 ml/min. The pump head used Cole-Parmer L/S 14 tubing with a 1/16-inch diameter made from a spallation-free tubing which goes by the trade name STA-PURE. The STA-PURE tubing can operate at an upper continuous pressure of 414 kPa (60 psi). Moreover, the peristaltic pump was selected because it is capable of pumping fluids with high solids content if desired, and can be run dry to flush the system between runs. An advantage of peristaltic pumps is that they do not have gears that can be worn down with time by particulates, which can act as an abrasive. The pulsations from the peristaltic pump were relatively low when operating at a flow rate of 5.93 ml/min. The uncertainty in the pressure drop when tested with a 6.89 kPa (1 psi) PX-26 pressure type from Omega was only 0.014 kPa (0.002 psi).

3.2 Test device

Much of the particulate fouling work was conducted with microchannel devices whose general form is illustrated in Fig. 5. The dimensions of the actual microchannels are given in Fig. 6 and Table 2. Throughout this document it will be referred to as the R9 chip. More details are provided in Perry (2007).

Figure 6 shows the location of the geometric variables used in Table 2 where $2b$ is the microchannel width, $2s$ is the fin thickness separating the microchannels and $2c$ is the depth of the microchannels. The total width and length of the microchannel array is 8 and 10 mm, respectively.

The R9 microchannels, shown in Fig. 5, were fabricated in silicon using deep reactive ion etching (DRIE) because
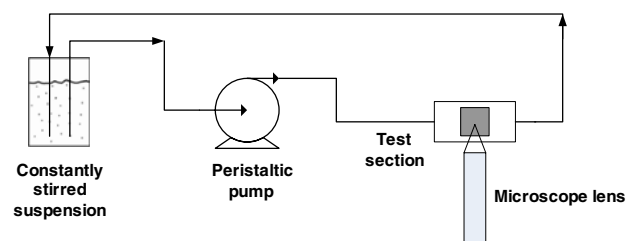
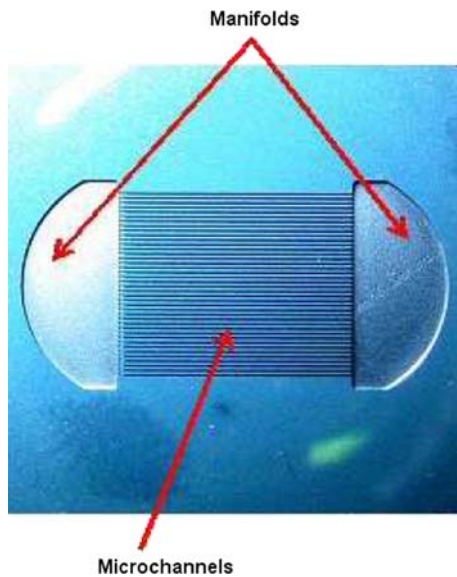**Fig. 4** Schematic of experimental flow loop used in microchannel fouling studies

Fig. 5 Example of silicon, parallel microchannels with inlet and outlet manifolds

Table 2 Channel geometries of R9 test device

Hydraulic diameter (μm)	2c (μm)	2b (μm)	2s (μm)	Pitch (μm)	Number of channels	Channel length (mm)
225	249	205	97	302	26	10

outlets of the channels have angles of 120°. Chips made from these designs are referred to as J2 chips. These chips were made from 6-inch silicon wafers with an unetched substrate thickness of 625 μm.

3.3 Micro-PIV studies

A μPIV (micro-PIV) system from TSI Incorporated was employed in this study. The schematic of the setup is shown in Fig. 8. The μPIV system was assembled around a Nikon Eclipse TE2000-S inverted microscope. The illumination beam was produced by a 90 mJ PIV Nd: YAG laser system from New Wave Research with a peak emission of 532 nm. The beam coming from the laser head is collimated by a set of diffusion filters to provide a uniform light source. The beam is then forwarded to an epi-fluorescent filter cube where part of the light is reflected upward towards a Nikon CFI Plan Fluor 10X objective lens with a numerical aperture of 0.30. The objective lens relays the light onto the microfluidic device, where it illuminates the entire flow volume. Fluorescent particles in the flow field absorb the light at $\lambda = 532$ nm and emit at $\lambda = 560$ nm. The light is then imaged by the objective lens and passed back through the filter cube where it is transmitted to a CCD camera (TSI 630047 PIVCAM 13-8 image capture system). The images from the camera are then downloaded to a personal computer for processing. A laser pulse synchronizer (TSI model 610034) was used to synchronize the laser and CCD camera to process the resulting image pairs so that velocity vectors and flow patterns could be ascertained. INSIGHT 3G software from
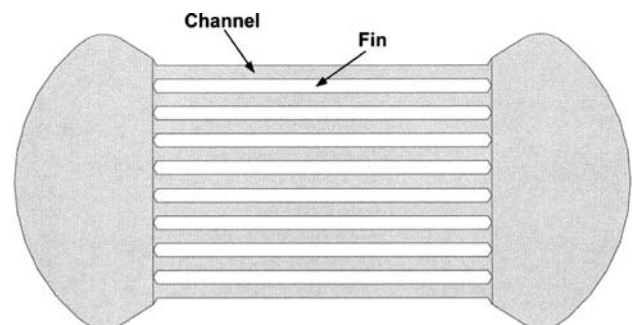
very high aspect ratios with straight sidewalls can be achieved with this etching technique; 8-inch wafers were used in the fabrication so the unetched substrates have a thickness of 725 μm. There are also inlet and outlet headers formed in the silicon. The backside of the header is rounded to help direct the flow and minimize stagnation regions. The silicon chip is sealed with a Pyrex cover by compression to form a fully functional microchannel device. The cover piece has the same overall dimensions as the silicon substrate. The thickness of the cover plate is 600 μm. The cover piece is laser drilled with two holes to match with the location of the inlet and outlet headers. The diameter of the plenum holes is 1.5 mm.

The other microchannels used in this study are discussed here. This design consists of only nine channels with a near equal fin and channel width of about 400 μm. The depth is 151 μm giving a hydraulic diameter of 220 μm, which is similar to the R9 chip previously discussed. The design of the chip is given in Fig. 7 and Table 3. The inlets and

Fig. 6 Schematic of the geometrical parameters of the R9 microchannels

Fig. 7 Diagram shows layout of microchannels consisting of nine channels with inlet and exit angles of 120°

Table 3 Channel geometries of J2 test device

Hydraulic diameter (μm)	2c (μm)	2b (μm)	2s (μm)	Pitch (μm)	Number of channels	Channel Length (mm)
220	151	407	393	800	9	10
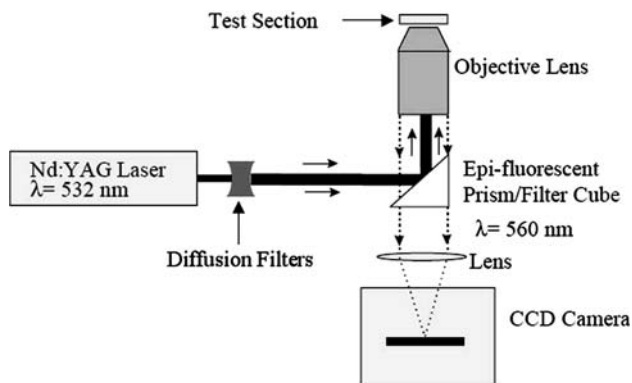
Fig. 8 Schematic diagram of the μPIV system, modified from Meinhart et al. (2000)

TSI Incorporated was used to process all the files captured by the μPIV system. All experiments used an interrogation area of 128 × 128 pixels.

Polystyrene microspheres from Invitrogen with a diameter of 1.0 μm were used. They are fluorescently tagged to excite and emit at peak values of 540 and 560 nm respectively. The particles in water, however, actually swell to a size of 1.1 μm. They came from the manufacturer with a concentration of 1.0×10^{10} particles/ml and were diluted by 10:1 with deionized water when used as tracers in the μPIV work. The fluid was run through the microchannels using a Genie Plus syringe pump from Kent Scientific.

Validation of the μPIV technique was performed using the R9 microchannels with a flow rate of 1.00 ml/min. The low-flow rate was used because the velocity in the channels at this value has the same velocity magnitude[1] in the header region when the microchannel test device is operating at 5.93 ml/min as used in the fouling studies. The shear rate was 4.2% less than theoretical calculations. The lower empirical velocity magnitudes can be attributed to the large measurement depth of 35 μm when using the 10X objective. Regardless of this, the low magnification objective was utilized because it enabled large areas in the header region of the microchannel test devices to be studied at one time.

---

[1] Velocity magnitude is defined as: $V_{mag} = \sqrt{V_x^2 + V_y^2}$, V_x and V_y are the velocities in the x and y directions respectively. V_x and V_y are perpendicular and parallel respectively to the channel entrances in the header region.

4 Results for alumina fouling of aggregated particles

### 4.1 Zeta potential adjustment of alumina particles and silicon channels

This section covers the experimental results obtained with the 1.25-μm average particle size alumina. The alumina particles with a pH of 3.0 are electrostatically attracted to the silicon surfaces of the R9 chip. This allows the fouling mitigation due to the electrostatic forces and the shear stress at the channel walls ($Re = 17$ in channels) from previous experiments to be decoupled since only the shear forces would be operating to minimize fouling.

The zeta potential versus pH for alumina and silicon particles is provided in Fig. 9. At a pH of 3.0 the absolute difference in potential between the two surfaces is 54.3 mV. This does, however, assume the zeta potential of the silicon channels can be correctly modeled with silicon particles. This is because the silicon microchannels were formed by a DRIE process, which is known to leave behind a polyfluorinated residue after etching that is very difficult to completely remove.

The zeta potential within the pH range of 2.5 and 3.5 for both particle types is for the most part steady. Therefore, a pH of 3.0 should provide a fairly constant potential difference between alumina and silicon even if the pH varies somewhat about the desired operating condition.

4.2 Alumina fouling in header regions

In numerous trials it was demonstrated that the shear stress at the channel walls is sufficiently large to prevent particulate deposition from occurring even when there is an electrostatic attraction between the alumina particles and
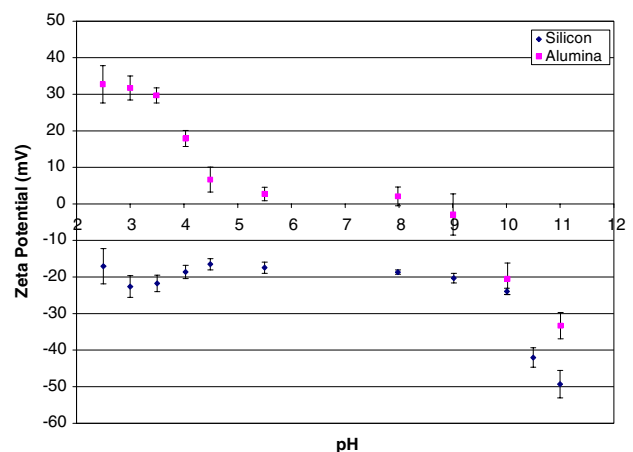
Fig. 9 Zeta potential versus pH for silicon and 1.25-μm alumina particles

the silicon microchannels. When operating at a flow rate of only 5.93 ml/min no fouling within the microchannels occurred. This flow rate is far below what is typically used in microchannels for heat dissipation. Flow rates used by Steinke (2005) ranged from 39 to 69 ml/min with the same test chip when used for heat transfer studies. The lack of fouling in the channels can be contrasted with the particle depositions that occurred within the inlet and outlet headers of the microchannel device. A visual comparison can be performed by looking at Figs. 10 and 11. Particulate fouling within the header regions is attributed to the low shear forces, which are unable to prevent particulate deposition from occurring.

The degree of aggregate coverage in the plenum increased with time, which was consistent across the entire header region. The aggregates formed only a single layer with clusters breaking off from the surface periodically. These particle deposits were observed in both the inlet and outlet header regions with a tendency for greater deposition at the inlet. The aggregates were shown to form deposition paths, which followed the natural streamlines of the fluid flow in the headers.

The average size of the alumina aggregates was estimated to be 24 ± 2 μm. This value was determined by taking the mean diameter of the aggregates with various geometries, which deposited in the header region. This was done using the digital microscope at a magnification of 500X when the alumina deposition was light enough to distinguish alumina clusters as being separate. The reason for the particle aggregation is not clear since the electrostatic forces have an energy barrier of over 1,000 kT which should be sufficient to prevent the particles from clustering together. Deviations from classic DLVO theory behavior
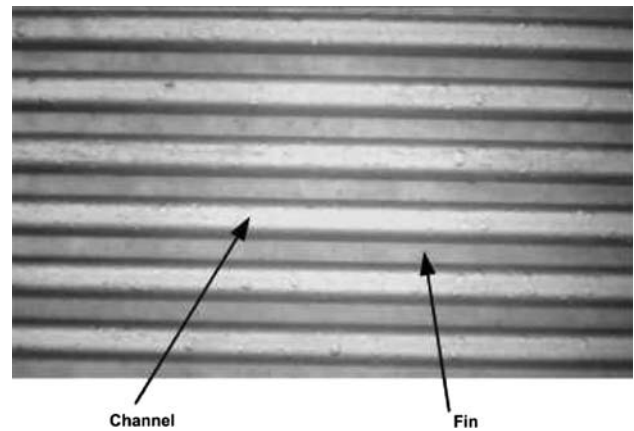
Fig. 11 Microchannels of R9 chip after 3 h. pH = 3.0, flow rate = 5.93 ml/min, Alumina particle conc. = 0.016 wt%

have been attributed to a number of causes. Two such reasons include discreteness of surface charge and surface roughness, Snoswell et al. (2005). Regardless of the exact reasons behind the particle aggregation the estimated mean aggregated particle size of 24 μm was used to determine why the alumina aggregates were depositing in the header region of the R9 chip but not in the microchannels.

The reason why the 1.25-μm alumina particles agglomerated in the fouling experiments can be understood by the fact that the particles were in the alpha form (corundum). This type of alumina is not soluble in water, strong acids or bases. This facilitated their aggregation since dispersal in the aqueous environment was not attainable while the solution was under constant shear while being stirred.

4.3 Wall shear stress in header and microchannels

The wall shear stress in the header region of the R9 chip was determined using the velocity profile versus distance information obtained with the μPIV. The data were taken in two regions of the header as shown in Fig. 10. The information of the first area (region 1) is given in Fig. 12 and that of the second area (region 2) is given in Fig. 13. The average wall shear stress in the two header regions is listed in Table 4.

The data show a larger shear stress further away from the channel entrances (region 2) because the flow is only bounded on one side in the x–y direction. Conversely, very close to the channel inlets the flow is bounded on two sides (region 1), which gives a lower average wall shear stress. In addition, the velocity magnitude in region 1 is less because it has two significant velocity components in both the x- and y-directions where in region 2 the velocity is mainly in the y-direction (velocity magnitude is at a maximum when the flow is dominant in one direction). The average wall shear stress in the microchannels was determined analytically
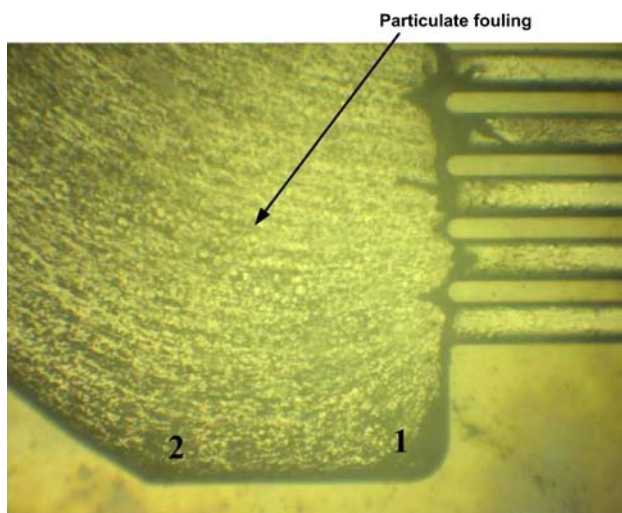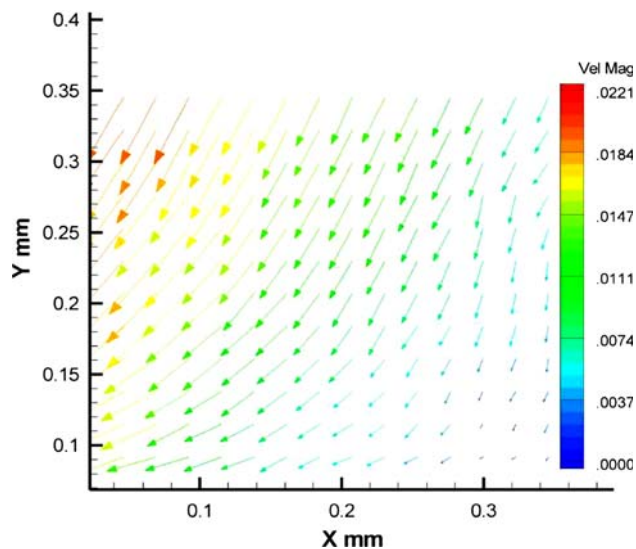

Fig. 10 Alumina particulate deposition within channel inlet header of the R9 chip after 3 h. pH = 3.0, flow rate = 5.93 ml/min, Alumina particle conc. = 0.016 wt%

Fig. 12 μPIV data of header region 1 of R9 chip. Region encompasses an area which is approximately 370 μm × 280 μm based on vector positions. Figure shows velocity magnitudes at an approximate distance of 52 μm from the surface in the header region

giving a value of 2.3 Pa. This is approximately 16 to 12 times greater than the shear stress in regions 1 and 2 respectively.

4.4 Controlling forces of particle aggregates at header and microchannel surfaces

Fouling occurred within the header region but not in the channels due to the competing forces of gravity and lift. This is shown in Table 5, which makes the comparison for
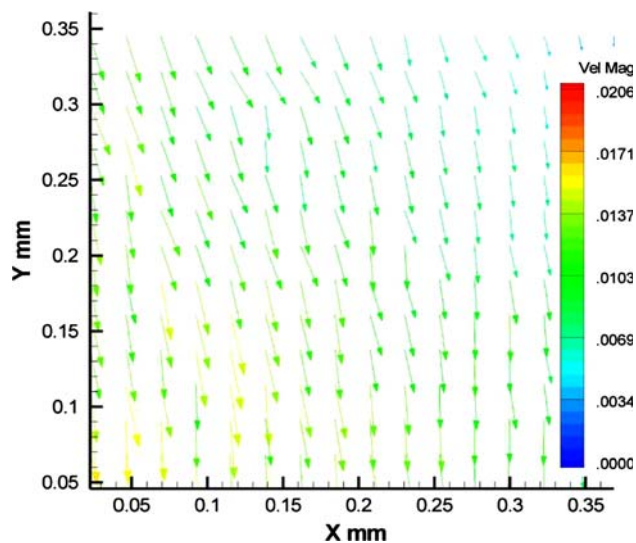

Fig. 13 μPIV data of header region 2 of R9 chip. Area encompasses a region which is approximately 350 μm × 300 μm based on vector positions. Figure shows velocity magnitudes at an approximate distance of 26 μm from the surface in the header region

Table 4 μPIV results in header regions and analytical calculations for microchannels of the R9 chip

Area	Average wall shear stress (Pa)
Region 1	0.14
Region 2	0.20
Microchannels	2.3

Table 5 Gravitational and lift forces in the R9 chip for 24 μm particle aggregates

Area of interest	Gravitational force (N)	Lift force (N)
Header region 2	2.1×10^{-10}	8.9×10^{-12}
Microchannels	2.1×10^{-10}	6.4×10^{-10}

Particle density is taken as that of the bulk value. Flow rate = 5.93 ml/min in test device

region 2 in the header, which had the larger average wall shear stress. In all cases a spherical aggregate was assumed for simplified calculations.

Within the header the gravitational force dominates and is about 24 times greater than the lift force[2]. Therefore, the particle aggregates will be able to settle on the bottom of the header. This explains in part why fouling was always observed in the R9 silicon header and not on the Pyrex cover, which enclosed this area of the microfluidic device. Conversely, within the microchannels the lift force is dominant and is approximately three times larger. The larger lift force prevents the particle aggregates from reaching the surface and depositing themselves.

When the electrostatic and van der Waals forces are considered, their impact is minimal. This is observed in Figs. 14 and 15 where the absolute values of the forces involved are considered for the situation shown in Fig. 1. Figure 14 compares the forces in region 2 of the header. In this case the gravitational force is greater than all other forces until a separation distance of 41 nm. Thereafter, the aggregated particles will be tightly held at the silicon surface by the attractive electrostatic forces. Figure 15 compares the forces involved within the R9 microchannels. Here the lift force is larger than the other forces at play until a separation distance of 30 nm. At this distance the positive electrostatic forces will dominate. However, fouling does not occur within the channels. This is because the alumina aggregates do not approach close enough to the silicon surface for particle deposition to occur.

---

[2] The gravitational force was based on the bulk density of the alumina particles. When aggregates grow there is a decrease in the aggregate density. Even if the density was reduced by a factor of 2 the gravitational force would still be eight times greater than the lift force in the header region.
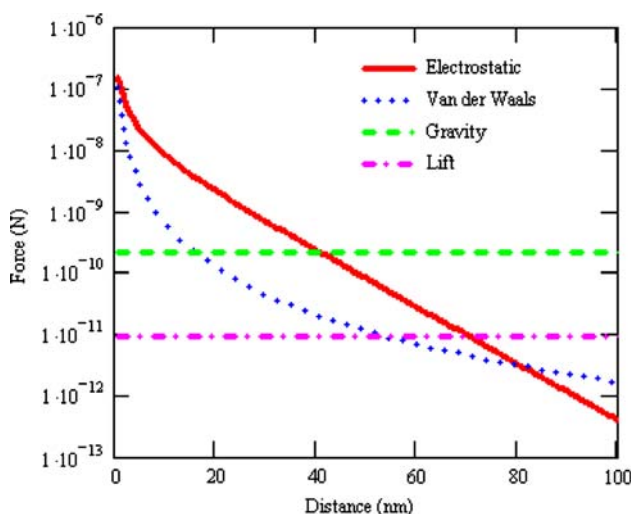
Fig. 14 Forces involved for different separation distances for a 24 μm alumina aggregated particle approaching a silicon surface in header region 2 of R9 chip. pH 3.0, τ_w = 0.20 Pa

4.5 Fouling with stable alumina particles

This section covers the experimental results obtained with the 248-nm average particle size alumina at a concentration of 0.032 wt%. The fouling behavior was observed for three regions of pH using the J2 chip with a flow rate of 5.93 ml/min (Re = 41 in channels). These include the following conditions:

(1) The alumina particles are electrostatically attracted to the silicon surface.
(2) The alumina particles experience electrostatic repulsion with the silicon surface.
(3) The alumina particles are near their isoelectric point.
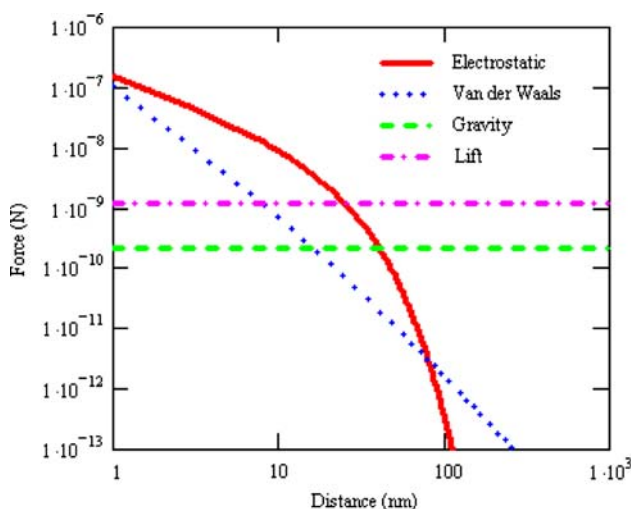

Fig. 15 Forces involved for different separation distances for a 24 μm alumina aggregated particle approaching a silicon surface in microchannels of R9 chip. pH 3.0, τ_w = 2.3 Pa

When the 248-nm alumina particles form a stable colloid the gravitational and lift forces are negligible compared to the DLVO forces. They are in fact several orders of magnitude lower. Consequently, the main focus of the discussion will center on the DLVO forces.

Unlike the alpha-type particles, which agglomerated in the fouling studies, the 248-nm particles were of the gamma form which is also known as active alumina. This form can more easily be dispersed and hence allowed for another aspect of alumina fouling to be studied.

4.6 J2 chip fouling with electrostatic attraction between alumina and silicon surfaces

At an operating pH of 3.0 the surfaces of the 248-nm alumina particles and the silicon test device are electrostatically attracted to each other with an absolute difference in zeta potential between them of 62.8 mV. Zeta potential versus pH for the 248 nm particles is given in Fig. 16. In addition, at this pH the alumina has a zeta potential of +40.1 mV, which according to DLVO theory will give a stable colloid with an energy barrier of over 200 kT between colloidal particles. This stability was observed by the fact that the particles at this pH did not aggregate together.

When running a concentrated 0.032 wt% alumina dispersion through the test device at a flow rate of 5.93 ml/min, no fouling was observed. At first glance this may seem odd since the particles are highly attracted to the silicon surface. However, it is well known that stable colloidal suspensions produce particle monolayers only, while further deposition is inhibited by unfavorable physico-chemical interactions between deposited and suspended particles, Yiantsios and Karbelas (1998). Several experiments have been performed with colloidal particles such as
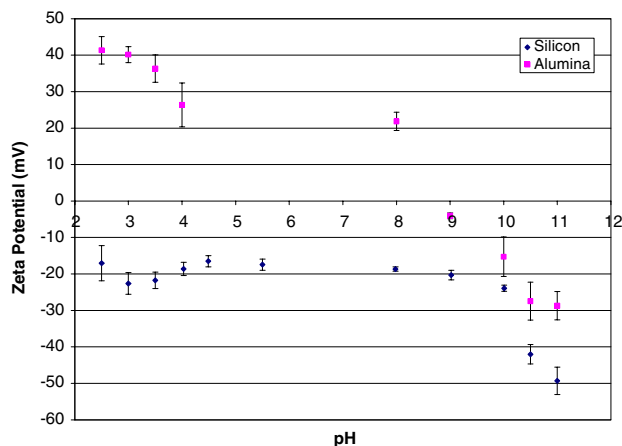

Fig. 16 Zeta potential versus pH for silicon and 248-nm alumina particles

latex and silica, which support this conclusion. Bowen and Epstein (1979) found in their studies that the maximum coverage never exceeded 10% for silica particles between 400 and 650 nm in size. In addition, Dabroś et al. (1983) discovered that a single 500 nm polystyrene sphere was able to block (other identical polystyrene spheres) for an area of about 20–30 times its geometrical cross-section. Experimental results will of course vary depending on conditions like double layer thickness, particle size and flow rate.

4.7 J2 chip fouling with electrostatic repulsion between alumina and silicon surfaces

At a pH of 10.0 and 11.0 the zeta potential for the 248-nm alumina particles had a repulsive force between themselves and the silicon surfaces of the J2 chip. At the lower pH the alumina particles themselves had a zeta potential of -15.3 mV, which gave them an energy barrier of 33 kT between particles, which was enough for the colloid to remain stable. Refer to Fig. 17 for the potential energy-distance curves for particle-particle interactions. An even greater stability was obtained when operating at a pH of 11.0, which had a zeta potential of -28.7 mV and an energy barrier of 113 kT between particles. This difference in the energy barrier was readily apparent. At a pH of 11.0 the stock solution with an alumina concentration of over 0.048 wt % would easily disperse after a couple minutes in the sonicator. However, at the lower pH of 10.0 it could take up to 10 min to obtain a stable colloid for use in the test loop.

At the lower pH of 10.0 the electrostatic energy barrier between the alumina particles and the silicon test chip was
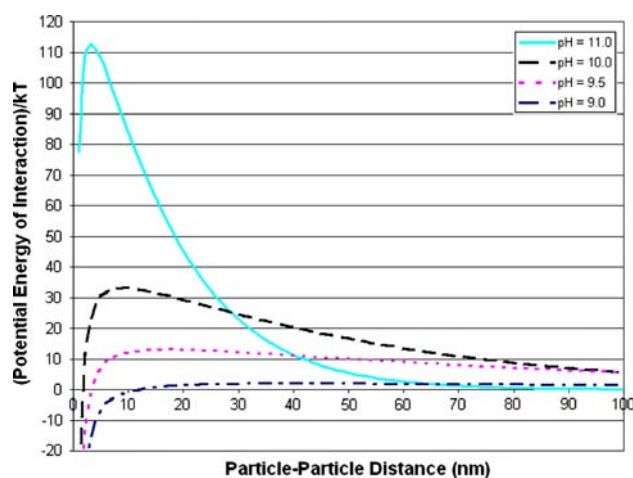

Fig. 17 Potential energy-distance plots for 248-nm alumina particles at different pH values. Plots are only valid up to a separation distance of 13 nm because of the limitations imposed by Derjaguin's approximation in the equations used

94 kT. This was sufficient to prevent fouling. However, even if fouling did occur, it would not be possible to perceive the deposited particles because only a monolayer would be formed on the silicon surfaces.

The pH was not raised above a value of 11.0. This is because a high OH^- concentration can etch away at the silicon. During zeta potential analysis of the silicon particles it was observed that between a pH of 10.5 and 11.0 the silicon particles reacted with the high concentration of KOH to form a silonal such as $Si(OH)_6^{2-}$, Seidel (1990). This caused the solution to go from slightly turbid to clear. The reason why this readily occurred after several hours (or only several minutes if the colloid was sonicated) is because the silicon particles have a high surface area to volume ratio. In addition, the gamma form of alumina is known to readily dissolve in strong acids and bases. This is in line with what was observed when the alumina particles were measured for zeta potentials. However because of this fact, experimental runs focused on pH values up to an upper limit of 10.0.

4.8 J2 chip fouling near the isoelectric point of the alumina particles

At an operating pH of 9.0–9.5, fouling within the header and channels was observed. The reasoning for this is that when operating close to the isoelectric point, the alumina colloid would become unstable and start to aggregate forming very large clusters. At this starting pH the energy barrier for particle-particle interactions was lowered to about 2.0 or 13 kT for pH values of 9.0 and 9.5, respectively[3]. This lowered energy barrier is enough for the individual alumina particles at a pH of 9.0 to starting forming doublets. The energy barrier of 13 kT may seem high enough to prevent alumina particles from aggregating (if only Brownian motion is considered). However, the alumina colloid was under a significant shear rate in the microchannels ($3{,}600$ s^{-1}), which can cause orthokinetic aggregation. In the absence of an energy barrier, the increased collision rate due to shearing is over six times larger. This helps explain this small discrepancy.

Since no buffers were used to control the pH it could drift to exist at the isoelectric point of the alumina particles during an experimental run or even obtain a charge opposite to the silicon surfaces. This would leave no repulsive electrostatic forces operating between the alumina and

---

[3] An approximate value for the energy barrier is given because the scaled separation distance, κa, for the 248-nm particles is only 1.04 at pH 9.0 and 1.69 at pH 9.5. At such a low value of κa the curvature of the surface elements will become important between the two interacting particles and Derjaguin's approximation loses its accuracy, which was used in the derivation of Eqs. 14 and 15.

silicon surfaces of the test device. Buffers were not used so that the electric double layer forces could be properly modeled since only single symmetrical electrolytes would be present.

The average shear stress in the header ranged from 0.29 to 1.30 Pa for regions 1 and 2 respectively of the J2 chip. These regions are shown in Fig. 18. The shear stress in the header close to the channel inlets (region 1) is much higher than what was observed for the R9 chip given in Table 4. This is because the larger channel widths provide a smaller restriction to flow. Conversely, the shear stress in the back of the header (region 2) is similar to what was obtained for the R9 chip. Yet it is slightly larger since the channel depth is less. This increase in velocity results so that the law of conservation of mass will be obeyed.

Calculations could be discussed concerning the lift and gravitational forces, which were at play. However, because the experiments were performed near the isoelectric point there were some confounding influences. Severe particle aggregation was present. This gave a large range in the aggregated particle size. In addition, the pH shifted to exist at the isoelectric point or past it, giving a positive charge on the alumina particles. Consequently, no absolute force balance could be obtained.

The particulate fouling in the header of the J2 chip is demonstrated by comparing Figs. 18 and 19. The latter figure shows that the particles, which were deposited were indeed small. Individual deposited particles could not be resolved even at a magnification of 500X. In addition, at this magnification, the CCD pixel size was 0.036 microns for a 1600×1200 pixel image size within the fouled header region.

It should be mentioned why the J2 chip was used to study the following phenomena instead of the R9 chip with the 248-nm alumina particles. The reason is that the R9 chip had a larger surface roughness of 1,400 Å which made
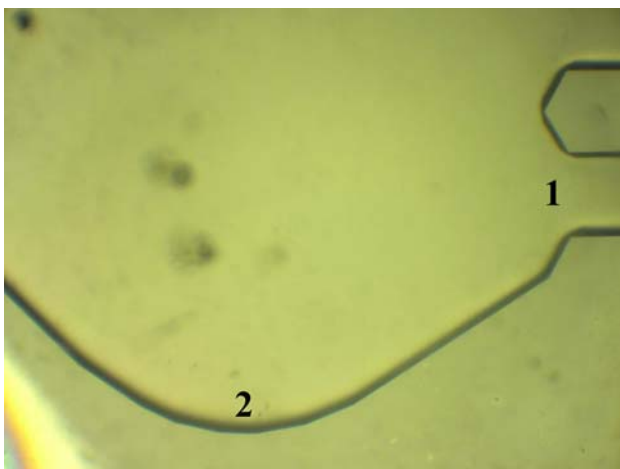

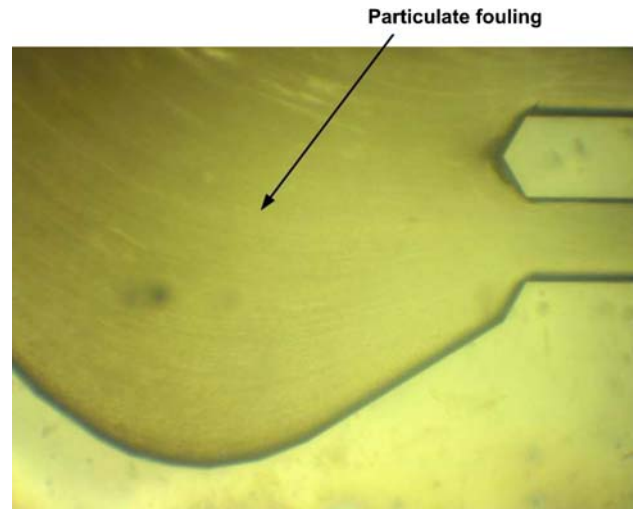**Fig. 19** Alumina particulate deposition within channel inlet header of J2 chip after 3 h. 0.032 wt% alumina, pH_{start} 9.5, flow rate = 5.93 ml/min. Magnification = X100

it difficult to observe the particle depositions with the digital microscope. Conversely, the J2 chip had a much lower surface roughness of 21 Å which did not mask the particle deposits. This was necessary for meaningful visualization studies.

5 Conclusions

An experimental investigation and theoretical analysis was undertaken to study the fouling in silicon microchannels used in IC chip cooling applications where the working fluid is water. The work focused on studying the characteristics of fouling and ways to mitigate its detrimental effects. The particulates used ranged from the colloidal size range up to tens of microns in size (for particle aggregates). By having a range in particle size the physicochemical interactions as well as the hydrodynamic forces were varied which gave different fouling characteristics. In addition, the pH was varied to adjust the electrostatic forces between the particles and the surfaces of the microchannel devices as well as the electrostatic forces of repulsion, which exist between similarly charged particles. The following conclusions can be drawn from the present work.

Fouling with large aggregated particles (≈ 24 μm) in typical, rectangular, microchannels used for heat dissipation (i.e. between 200 and 300 μm per side) is extremely unlikely because of the high shear stresses involved even at a low flow rate of 5.93 ml/min (velocity of 0.64 m/s in channels, $Re = 17$). This is still the case when particles are electrostatically attracted to the microchannel surface. It is the large lift forces involved which are responsible for inhibiting particle deposition. This will occur when the

Fig. 18 Header of J2 chip prior to experimental run

particles have sufficient size for the lift force to overcome the gravitational force.

The channel header is quite susceptible to particulate fouling. This is because of the low shear stress at the wall in the header region. In contrast, it is fortuitous that the microchannels do not possess the same fouling characteristics as the headers. This is especially the case since they have the smallest geometrical constraints in a microfluidic device.

Even when there is a large concentration of particulates flowing through a microchannel device, a high electrostatic energy barrier between the particles themselves will prevent fouling. This is true for particles in the nanometer regime (i.e. 248 nm). In addition, a large energy barrier between the particles and the microfluidic surfaces will help prevent fouling as long as the particles have good colloidal stability.

Proper pH adjustment is critical to prevent fouling in a microchannel test device. If the particles exist close to their isoelectric point severe fouling can occur. However, care must be taken not to make the aqueous medium too corrosive (basic). This is because the high concentration of OH^- ions will etch away at the silicon surfaces over time. In fact the etch rate will increase at elevated temperatures. This is supported by the thesis work and the experiments of Seidel (1990).

When performing fouling studies on silicon substrates it is advantageous to have a low surface roughness so that it does not unintentionally mask particles that have deposited. Consequently, care must be taken during the silicon etch process to prevent increased surface roughness from occurring. Moreover, a smoother surface should aid in the removal of a particle once it has been deposited, as indicated by Hubbe (1984).

The headers in a microfluidic device should be well rounded and designed so that there are no stagnation regions or areas where the flow will make abrupt changes in direction. A large change in the velocity in the forward direction of flow, to a lateral one will reduce the velocity magnitude as well as the local wall shear stress.

The experimental evidence suggests that if a microfluidic device has a large header feeding a number of smaller microchannels, it may be beneficial to etch the header to a smaller depth than the channels. This will allow for an increased velocity, which will translate into a larger shear stress on the surfaces of the header. This will in turn help to mitigate particulate fouling. This may be done by using a technique called one-step two-level etching (OSTLE), Grande et al. (1987). With this technique, the mask used for the channels would be made of a material, which erodes at a faster rate than the masking layer used for the header. This would be especially helpful when high flow rates are not being run through the device.

References

Abulnaga BE (2002) Slurry systems handbook, chap 9. McGraw-Hill, New York

Benzinger U et al (2005) Anti fouling investigations with ultrasound in a microstructured heat exchanger. In: Proceedings of the 6th international conference on heat exchanger fouling and cleaning challenges and opportunities. Kloster Irsee, Germany

Bergendahl J, Grasso D (2000) Prediction of colloid detachment in a model porous media: hydrodynamics. Chem Eng Sci 55:1523–1532

Bowen BD, Epstein N (1979) Fine particle deposition in smooth parallel-plate channels. J Colloid Interface Sci 72:81–90

Dabroś T et al (1983) Direct method for studying particle deposition onto solid surfaces. Colloid Polym Sci 261:694–707

Derjaguin BV, Landau LD (1941) Theory of the stability of strongly charged lyophobic sols and the adhesion of strongly charged particles in solutions of electrolytes, Acta Physicochim URSS 14:633–662

Grande WJ et al (1987) One-step two-level etching technique for monolithic integrated optics. Appl Phys Lett 51:2189–2191

Gregory J (1981) Approximate expressions for retarded van der Waals interaction. J Colloid Interface Sci 83:138–145

Hogg R, Healy TW, Fuerstenau DW (1966) Mutual coagulation of colloidal dispersions. Trans Faraday Soc 62:1638–1651

Holmberg K (2001) Handbook of applied colloid & surface chemistry, Chaps. 9, 10. Wiley, New York

Hu T (2004) Slurry flow control: improving yield rates on existing CMP tools. Cleanrooms mag, vol 18, issue 4, April 2004. Available at http://cr.pennnet.com/display_article/203332/15/ARTCL/none/none/1/Slurry-flow-control:-Improving-yield-rates-on-existing-CMP-tools/

Hubbe MA (1984) Theory of detachment of colloidal particles from flat surfaces exposed to flow. Colloids Surf 12:151–178

Kakaç S (1987) Handbook of single-phase convective heat transfer, chap 3. Wiley, New York

Kern W (1993) Handbook of semiconductor wafer cleaning technology: science, technology, and applications, chap 4. Noyes Publications, Berkshire

Leighton D, Acrivos A (1985) The lift on a small sphere touching a plane in the presence of a simple shear flow. J Appl Math Phys (ZAMP) 36:174–178

Marshall JS (2007) Particle aggregation and capture by walls in a particulate aerosol channel flow. J Aerosol Sci 38:333–351

Meinhart CD, Wereley ST, Gray MHB (2000) Volume illumination for two-dimensional particle image velocimetry. Meas Sci Technol 11:809–814

Niida T, Kousaka Y, Furukawa T (1989) Removal of adhering particles of polystyrene latex and iron oxide on a wall by shear flow in water, Particle and Particle. Syst Charact 6:69–73

Ohshima H (1994) Simple expression for Henry's function for the retardation effect in electrophoresis of spherical colloidal particles. J Colloid Interface Sci 168:269–271

Ohshima H, Healy TW, White LR (1982) Improvement on the Hogg-Healy-Fuerstenau Formulas for the interaction of dissimilar double layers. J Colloid Interface Sci 89:484–493

O'Neill ME (1968) A sphere in contact with a plane wall in a slow linear shear flow. Chem Eng Sci 23:1293–1298

Perry JL (2007) Fouling and its mitigation in silicon microchannels used for IC chip cooling. PhD thesis, Rochester Institute of Technology, Rochester

Seidel H et al (1990) Anisotropic etching of crystalline silicon in alkaline solutions-I. Orientation dependence and behavior of passivation layers. J Electrochem Soc 137:3612–3626

Snoswell D et al (2005) Colloid stability of synthetic titania and the influence of surface roughness. J Colloid Interface Sci 286:526–535

Steinke ME (2005) Single-phase liquid flow and heat transfer in plain and enhanced silicon microchannels. PhD. thesis, Rochester Institute of Technology, Rochester

Van de Ven T (1989) Colloidal hydrodynamics, chap 1. Academic Press, New York

Verwey EJW, Overbeek J Th G (1948) Theory of the stability of lyophobic colloids. Elsevier, Amsterdam

Yiantsios SG, Karabelas AJ (1995) Detachment of spherical micro-particles adhering on flat surfaces by hydrodynamic forces. J Colloid Interface Sci 176:74–85

Yiantsios SG, Karabelas AJ (1998) The effect of gravity on the deposition of micron-sized particles on smooth surfaces. Int J Multiph Flow 24:283–293

Yiantsios SG, Karabelas AJ (2003) Deposition of micron-sized particles on flat surfaces: effects of hydrodynamic and physico-chemical conditions on particle attachment efficiency. Chem Eng Sci 58:3105–3113